

Critical Appraisal of Integrated CFD/Surface Roughness Models for Additive Manufactured Swirl Burners

1 **Rashed Al-ajmi**¹

2 Associate Professor

3 Mechanical Power Engineering Department, College of Technological Studies,

4 PAAET, Shuwaikh 70654, Kuwait

5 rm.alajmi@paaet.edu.kw

6

7 **Mohammed Al-Shaghdari**

8 Graduate Studies Specialist

9 College of Engineering, Qatar University, PO Box 2713, Doha, Qatar

10 malshaghdari@qu.edu.qa

11

12 **Burak Goktepe**

13 Research Associate

14 Cardiff University School of Engineering, Cardiff, Wales CF24 3AA, UK

15 GoktepeB@cardiff.ac.uk

16 ASME Membership (if applicable)

17

18 **Ianos Psomoglou**

19 PhD Graduate

20 Cardiff University School of Engineering, Cardiff, Wales CF24 3AA, UK

21 Psomogloul@cardiff.ac.uk

22 ASME Membership (if applicable)

23

24 **Phil Bowen**

25 Professor

26 Cardiff University School of Engineering, Cardiff, Wales CF24 3AA, UK

27 BowenPJ@cardiff.ac.uk

28 ASME Membership (if applicable)

29

30

¹ Corresponding author information can be added as a footnote.

31 ABSTRACT

32

33 *Additive manufacturing (AM) technology can create complex parts that are otherwise impractical to*
34 *manufacture by traditional methods. However, the process often results in rough and irregular*
35 *surfaces that can affect performance. In this study, Computational Fluid Dynamics (CFD) is*
36 *considered as a tool to optimise component design for use in applications such as a gas turbine.*
37 *However, modelling the interactions between turbulent flows and Additive Manufacture (AM)-*
38 *generated wall roughness affect the predictive capability of numerical models due to difficulty in*
39 *thoroughly characterising rough wall texture. To progress towards addressing this issue, this study*
40 *aims to appraise two common wall roughness approaches within the RANS framework: the*
41 *modified 'law-of-the-wall' and roughness-resolving approaches. The modified law-of-the wall is*
42 *based on the correlation that converts the measured surface roughness parameters to the*
43 *equivalent sand-grain roughness height. The second approach involves the resolution of the*
44 *roughness elements within the computational grid. The simulations were compared against the*
45 *velocity data published for the burner with AM swirl nozzle inserts of different surface finishes. At*
46 *this stage of development, the Realizable $k-\epsilon$ turbulence model was selected for all the CFD*
47 *simulations. The results show that the roughness-resolving approach was better suited than the*
48 *modified law-of-the wall correlation, demonstrating good agreement with the experimental velocity*
49 *data, predicting the velocity shift to the center. The model also revealed the shortened recirculation*
50 *zone with increasing surface roughness, which is important in predicting flame stability and*
51 *emissions performance to be studied subsequently.*

52

53 Keywords

54 *Additive-Manufacturing, Surface Roughness, Swirl Burners and Computational Fluid Dynamics,*
55 *Isothermal Flow*

56

57

58

59

60 **1. INTRODUCTION**

61

62 Additive manufacturing (AM) has been identified as a disruptive technology
63 that enables the creation of complex geometries and structures that were
64 previously impractical to manufacture using conventional methods. This novel
65 technology is increasingly being recognized in the gas turbine industry as it offers
66 numerous benefits including time-efficiency, cost-effectiveness, and
67 unprecedented potential for improving the use of renewable low- and zero-carbon
68 fuels like hydrogen, ammonia, and biofuels [1]. For instance, Ansaldo has
69 developed a new sequential burner, called the Centre Body Burner, for
70 implementation into the GT36 H-class gas turbine using AM technology. The new
71 burner surpassed state-of-the-art hardware regarding emission reduction, fuel
72 flexibility, and load flexibility [2]. Other additive solutions for industrial Gas Turbines
73 (GTs) are rapid prototyping, on-site repair service, developing advanced-cooling
74 structures, and mass production [3].

75 The adoption of AM technology in the gas turbine industry has been limited
76 due to a few challenges, despite its numerous benefit [4]. One of the major
77 challenges is the rigorous design requirement for gas turbine parts, which
78 demands a comprehensive understanding of AM process and material properties.
79 AM processes produce typically higher surface roughness compared to
80 conventional processes due to the layer-upon-layer manufacturing technique and
81 the complex nature of particle deposition and fusion [5]. A review study
82 demonstrated that rough surfaces can significantly affect the flow and heat transfer
83 by modulating boundary layer flows [6]. This can compromise the aerodynamic

84 efficiency, structural integrity, and overall performance of gas turbine parts.
85 Another study has reviewed the interactions of turbulent flows with rough surfaces,
86 highlighting roughness-induced effects of increased pressure drop, induced
87 boundary layer transition, and enhanced heat transfer [7]. A series of experiments
88 were conducted on both AM and traditionally machined swirler inserts in a
89 representative gas turbine combustor [8]. The findings demonstrated the
90 modification of mean velocity, turbulence statistics and NOx emissions with
91 surface roughness height. To gain a thorough understanding of the rough wall-
92 turbulent flow interactions involved, it is essential to conduct comprehensive
93 investigations using both experimental and numerical methods. While experiments
94 are crucial, CFD can provide more detailed information, particularly of interest in
95 cases where experiments are not feasible.

96 CFD is widely used for designing and optimising Gas Turbine components,
97 employing a range of turbulence models for predicting the key features of heat and
98 flow transfer within reasonable accuracy. Among all other models, Reynolds-
99 Averaged Navier-Stokes (RANS) models are still being adopted in industrial
100 applications due to its relatively low computing power requirements and ease of
101 use. Many researchers have demonstrated good agreement with experimental
102 data to predict swirling flow structures, typically encountered in GTs, within the
103 RANS approach [9–11]. However, surface roughness adds further complexity and
104 uncertainty to numerical flow simulations due to the variations of roughness
105 geometry and scale in near-wall regions [7]. In the literature, three main

106 approaches consider surface roughness effects in CFD models, each with
107 limitations and requirements.

108 The first approach is to modify the boundary condition on the walls to ensure
109 the downward shift in the logarithmic velocity due to roughness elements [7, 12].
110 This approach is based on the modification of the standard law-of-the-wall for
111 smooth surfaces. Many researchers have used this approach with RANS
112 turbulence models in a variety of applications [13, 14]. However, this method has
113 its challenges as it assumes a correlation between measured surface roughness
114 parameters (e.g. the measured peak-to-valley roughness heights, R_z) and
115 equivalent sand-grain roughness (k_s). The lack of a universal correlation makes it
116 difficult to accurately apply this method, despite many proposed correlations [15,
117 16].

118 The second approach is the "discrete element" approach that has shown
119 promise in overcoming these limitations [6]. This approach introduces an extra
120 term into the governing equations to account for the flow restriction caused by
121 surface roughness, as well as the drag and heat transfer on roughness elements
122 [17]. One of the advantages of this approach is that it is not correlated to the
123 Reynolds analogy, making it applicable to both uniform and non-uniform surface
124 roughness [18]. However, it is not well-suited for use in three-dimensional
125 unsteady flow fields, which has hindered its use in GT-related flows.

126 The third approach involves fully resolving surface roughness within the
127 computational grid, which theoretically offers the ultimate way to investigate the
128 effects of surface roughness. However, the computational requirements of the

129 simulation domain often limit the applicability of this method due to a high ratio
130 between the associated geometry and roughness length scales [19, 20].

131 In order to meet the design requirements of the GT combustors made
132 through AM, it is very important to predict turbulent flow-rough wall interactions.
133 There is a clear need to develop reliable and robust models that require less
134 computational demand but can still accurately predict AM-induced surface
135 roughness affects. In this study, two different roughness approaches were
136 compared within the RANS framework applied to an unconfined, atmospheric
137 premixed burner with different AM swirl inserts. The paper describes the process
138 of applying wall roughness approaches to CFD simulations. The study conducted
139 a mesh independence analysis to ensure that the results were not dependent on
140 the grid. Finally, the paper discusses the ability of the selected approaches to
141 predict the effects of roughness elements on the mean characteristics of swirling
142 flows.

143 2. METHODOLOGY

144 The CFD simulations were performed for a swirling premixed burner
145 equipped with AM swirl inserts of different surface roughness heights. The study
146 used a commercial software ANSYS Fluent v.2023.R1. Two wall roughness
147 modelling approaches were compared and validated in this study: the modified
148 law-of-the-wall and roughness resolving approaches. The RANS approach with
149 the realizable $k-\epsilon$ closure model was used to predict the time-averaged motions of
150 turbulent swirling flows in the computational fluid domain. This model is widely
151 used in the research studies of turbulent swirling flows with a good prediction of
152
153

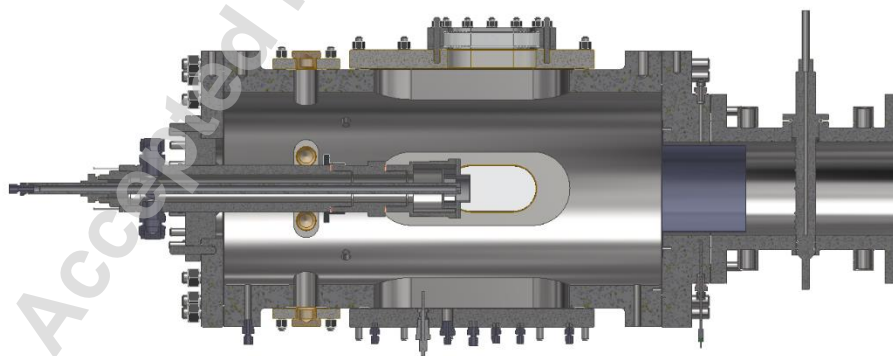
154 measured velocity profiles [21–24]. Scalable wall function and enhanced wall
155 treatment were selected based on the wall roughness approaches adopted and its
156 requirements for wall-bounded turbulent flows. In order to maintain the boundary
157 layer mesh entirely within the log-law region and avoid the singularity issues arising
158 from finer mesh for the modified law-of-the-wall approach, the scalable wall
159 function was used in the CFD simulations. Moreover, enhanced wall treatment was
160 applied to the wall-resolved RANS simulations, to ensure the resolution of the
161 viscous layer on the rough surfaces and the application of the wall functions to the
162 rest.

163

164 **2.1 Computational Domain and Grid**

165

166 Cardiff University Gas Turbine Research Centre's High Pressure Optical
167 Combustor (HPOC) used in the numerical simulations houses a swirl burner that
168 consists of a modular solid body with radial-tangential inserts giving a geometrical
169 swirl number of 0.8, as shown in Fig. 1.



170

171 **Fig. 1** A cut-through geometrical representation of HPOC rig without flame confinement tube.

172 The geometrical swirl number (S_g) has been calculated using the equation
173 provided below [25]:

$$174 \quad S_g = \frac{A_{noz} r_{tan}}{A_{tan} r_{noz}} \left(\frac{Q_{tan}}{Q_{tot}} \right)^2 \quad (1)$$

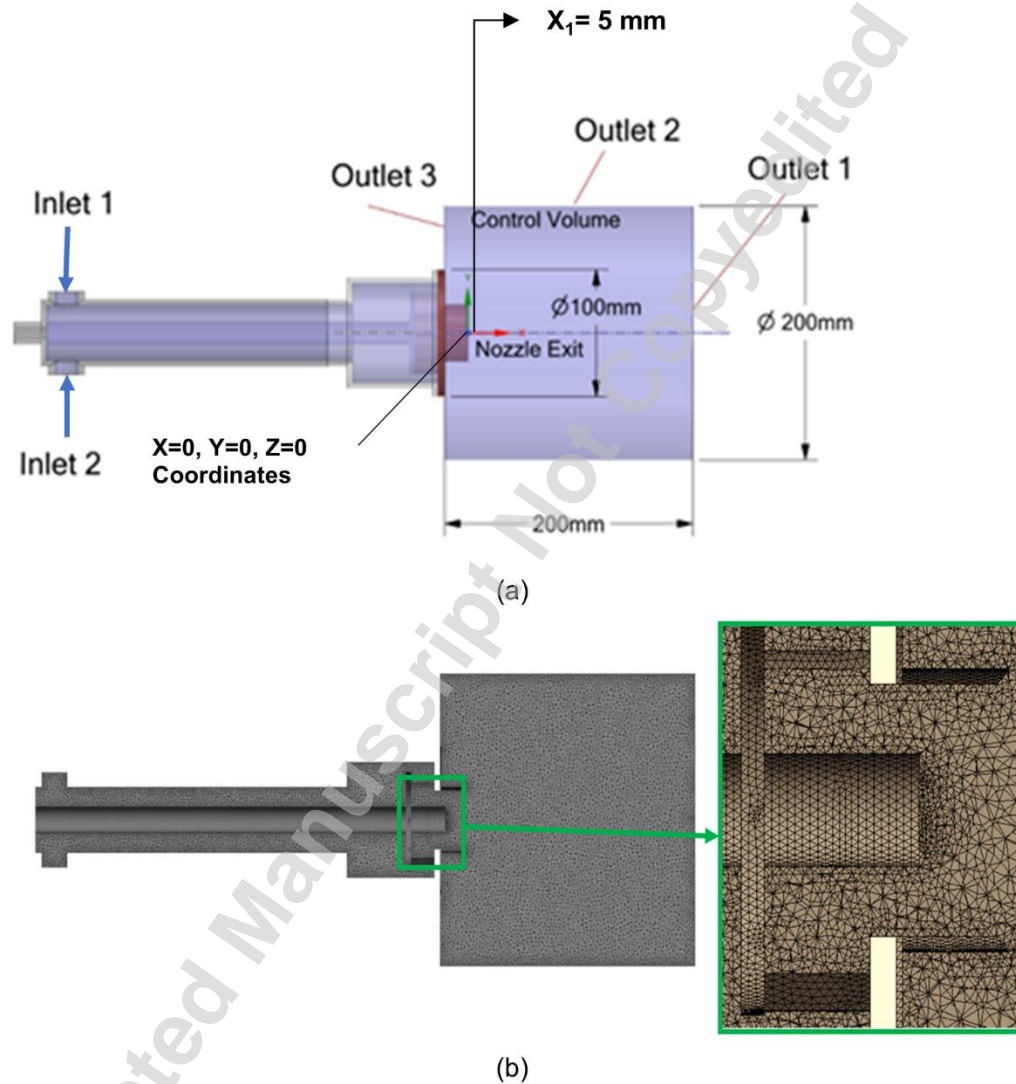
175 The terms A_{noz} and A_{tan} refer to the exit area of the burner nozzle and the area of
176 the tangential inlet, respectively. The variables r_{tan} and r_{noz} represent the effective
177 radius of the tangential inlet and the radius of the burner exit nozzle, respectively.
178 Additionally, Q_{tan} indicates the tangential flow rate, while Q_{tot} signifies the total flow
179 rate.

180 The setup involves the use of turbulent swirling flows, which emerge from
181 the swirl inserts and then stabilize on an annular bluff body with an outer diameter
182 of 18 mm. The flow then expands into the rig through a nozzle of 40 mm inner
183 diameter. Nine swirl vanes, aligned in tangential and radial configurations, are
184 used to impart the swirling flow into the airflow. This setup is commonly known as
185 the generic swirl burner and has been widely used in many studies before [25, 26].

186 To simulate the flow dynamics in the rig, the computational domain was
187 constructed based on the assumption that flow is unconfined as the confinement
188 ratio is low at 0.14. This simplification has been implemented to ensure a smooth
189 and efficient mesh generation and reduce allocated computational time. Fig.
190 2 presents a 3-D computational domain of the unconfined generic swirl burner with
191 the unstructured mesh built-in. It consists of a plenum chamber feeding ambient
192 air into the burner via two inlets, a swirl burner and an annular fluid volume with
193 three outlets. In Fig.2 (a), X_1 represents the spatial location 5 mm above the burner
194 exit, where CFD data was validated against experimental data.

195

196



197

198 **Fig. 2** (a) Computational domain with dimensions and tagged boundaries, and (b) Built-in

199 tetrahedral mesh.

200 A grid independency study was conducted with three tetrahedral mesh sizes

201 (ΔX) (3 mm, 2.25 mm, 1.5 mm), giving a total number of cells ranging from 0.87 x

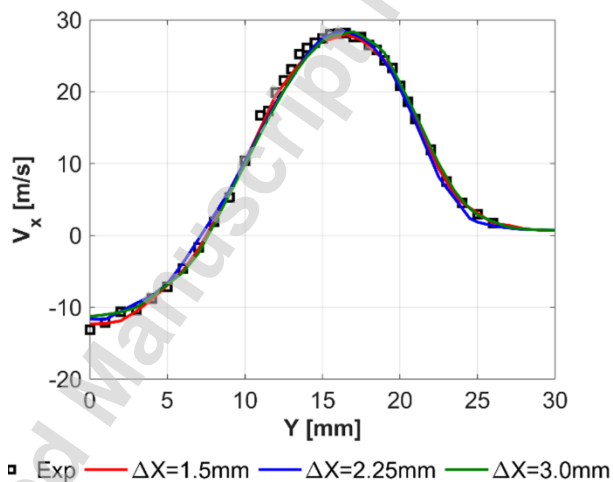
202 106 to 3.7 x 106, as shown in Table 1.

203 Table 1 Tetrahedral mesh size used for the grid sensitivity study.

Mesh Element Size (ΔX)	3 mm	2.25 mm	1.5 mm
Number of Nodes	1247764	2300339	5200453
Number of Cells	870168	1619654	3695454

204

205 To determine the ideal mesh size for the simulations, the axial velocity
 206 profile was used as a representative parameter and compared to that obtained
 207 from the experimental study at $X_1=5$ mm [8]. The mesh independency test results
 208 are provided for the modified law-of-the-wall approach applied to the 8M swirler as
 209 shown in Fig. 3.



210

211 **Fig. 3** Grid independency study for the modified law-of-the-wall applied to the 8M swirler.

212 The mean axial velocity profile of the swirling flow is predicted well by the realizable
 213 turbulence model, which matches the peak velocities and recirculation zones of
 214 the measured values. Due to the minimum discrepancy between the experimental
 215 and simulation results, a grid size of 1.5 mm was selected for performing all other
 216 CFD cases.

217 For this research, a numerical model was used to examine the performance
 218 of three swirl inserts that were fabricated using AM and had different surface
 219 finishes. These inserts were previously identified as "8R" (raw AM swirler), "8G"
 220 (grit blasted AM swirler), and "8M" (Traditionally machined swirler) in a study
 221 conducted by Runyon et al., [8]. For each swirl burner and its five separate
 222 surfaces, R_z values were measured by averaging the ten-point surface roughness,
 223 tabulated in Table 2. Detailed information on characterisation of surface roughness
 224 can be found in [8]. For all simulation cases, Table 2 values were used for k_s input.

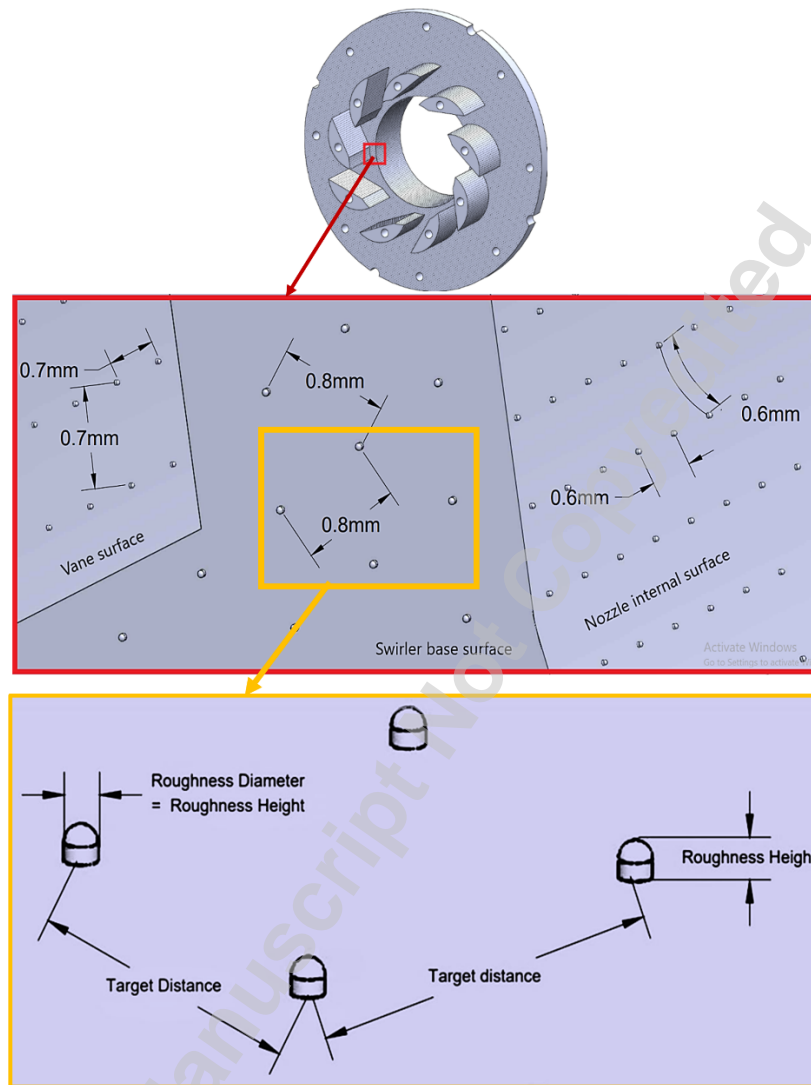
225

226 Table 2 Statistics of the surface roughness based on R_z .

Swirl Inserts	Surface Diameter [μm]				
	Nozzle Internal surface	Swirler Base surface	Vanes curved surfaces	Flat Vanes surfaces	Vanes curved surfaces 2
8R	53.61	78.11	50.01	54.06	54.06
8G	35.5	49.57	31.15	31.06	33.54
8M	8.96	11.21	6.12	9.07	9.07
Target Distance [μm]					
8M,8G,8R	600	800	700	700	700

227

228 The second approach resolves roughness elements within the
 229 computational grid by using enhanced wall treatment. Fig. 4 shows the geometrical
 230 representation of the surface roughness elements extracted upon the smooth wall
 231 surfaces of the swirl inserts.



232

233

Fig. 4 3D-CAD model of the swirl burner surfaces with built-in roughness elements and the roughness parameters.

234

235

236

The roughness elements were aligned uniformly across the wall surfaces within a distance, so-called target distance shown in Table 2. The target distance was set to obtain maximum achievable density of roughness elements, considering the allocated computational capacity.

237

238

239

240

241

242

243 **2.2 Governing Equations**

244

245 In the Reynolds averaging approach, the governing equations for an
246 incompressible Newtonian fluid are formulated as [27]:

$$247 \quad \frac{\partial u_i}{\partial x_i} = 0 \quad (2)$$

$$248 \quad \frac{\partial}{\partial t}(\rho u_i) + \frac{\partial}{\partial x_j}(\rho u_i u_j) = -\frac{\partial p}{\partial x_i} = \frac{\partial}{\partial x_j} \left(\mu \left(\frac{\partial u_i}{\partial x_j} + \frac{\partial u_j}{\partial x_i} \right) - \rho \overline{u_i' u_j'} \right) \quad (3)$$

249 where u_i and u_i' are the mean and fluctuating velocity components, respectively, t
250 is time, p is pressure and μ is the dynamic viscosity.

251 This approach uses Boussinesq hypothesis to relate the Reynolds stresses
252 to mean velocity gradient:

$$253 \quad -\rho \overline{u_i' u_j'} = \mu_t \left(\frac{\partial u_i}{\partial x_j} + \frac{\partial u_j}{\partial x_i} \right) - \rho \frac{2}{3} k \delta_{ij} \quad (4)$$

254 where μ_t is the turbulent viscosity, k is the turbulent kinetic energy and δ_{ij} the
255 Kronecker delta tensor.

256 For two equations models, the turbulent viscosity is determined from a
257 knowledge of k and the turbulent dissipation rate ε in the following relation:

$$258 \quad \mu_t = C_\mu \rho \frac{k^2}{\varepsilon} \quad (5)$$

259 In comparison to other k - ε turbulence models, the realizable k - ε model uses
260 a variable C_μ proposed by Reynolds.

261 **2.3 Roughness Modelling**

262

263 The first strategy applies a roughness function that modifies the standard
264 law-of-the-wall for smooth walls, proposed by Clauser [28] and Hama [29]. The

265 roughness function (f_r) shifts the logarithmic velocity profile downward, as
 266 formulated in Ansys Fluent [30]:

$$267 \quad u^+ = \frac{1}{\kappa} \ln(Ey^+) - \Delta B \quad (6)$$

268 where $u^+ = \frac{u}{u^*}$ is the non-dimensional velocity, $u^* = \sqrt{\frac{\tau_w}{\rho}}$ is the friction velocity, τ_w
 269 is the wall-shear stress, ρ is the fluid density, κ is the von Karman constant
 270 (0.4187), E is the constant (9.793), $y^+ = \frac{yU^*}{\nu}$ is the non-dimensional wall normal
 271 distance to the wall, ν is the kinematic viscosity and $\Delta B = \frac{1}{\kappa} \ln(f_r)$ is the additive
 272 constant in the log-law. f_r can be expressed as a function of the non-dimensional
 273 roughness height or so-called as roughness Reynolds number:

$$274 \quad k_s^+ = \frac{k_s u^*}{\nu} \quad (7)$$

275 where k_s is the physical roughness height or so-called as sand-grain roughness
 276 height.

277 Various roughness functions have been reviewed in literature [7]. Ansys
 278 Fluent adopts Cebeci and Bradshaw formulations [31] based on Nikuradse data
 279 [32], which calculates f_r for each of three distinctive roughness regimes:
 280 hydraulically smooth, transitionally rough, and fully rough regime.

- 281 • For the hydrodynamically smooth regime ($k_s^+ \leq 2.25$):

$$282 \quad \Delta B = 0 \quad (8)$$

- 283 • For the transitional regime ($2.25 < k_s^+ \leq 90$):

$$284 \quad \Delta B = \frac{1}{\kappa} \ln \left[\frac{k_s^+ - 2.25}{87.75} + C_s k_s^+ \right] x \sin\{0.4258(\ln k_s^+ - 0.811)\} \quad (9)$$

285

286 where C_s is a roughness constant. For tightly packed, uniform sand-grain
287 roughness, $C_s=0.5$. Higher values imply the departure from the uniform sand-grain
288 roughness. In this study, C_s were set to 1 for the wall boundary conditions of
289 modified law-of-the-wall models.

290 • For the full rough regime ($k_s^+ > 90$):

$$291 \quad \Delta B = \frac{1}{\kappa} \ln(1 + C_s k_s^+) \quad (10)$$

292 A simple algorithm was used to correlate, R_z shown in Table 2 to k_s [33]:

$$293 \quad k_s = 0.978R_z \quad (11)$$

294 2.4 Boundary Conditions

295 The boundary conditions were chosen to match those of the experimental
296 study in [8], in order to confirm the numerical accuracy of the physical model. For
297 each inlet, a mass flow boundary condition was used with a prescribed flow rate of
298 0.00805 kg/s and an air temperature of 573 K, which corresponds to an
299 equivalence ratio of 0.55 for a methane-air mixture. At the inlets, turbulence
300 intensity and hydraulic diameter were set to 4.72% and 0.02 m, respectively.
301 Pressure outlet boundary conditions were applied at the outlets, with turbulence
302 intensity set to 10% and hydraulic diameters specified for each outlet. The wall
303 domains were assigned a no-slip wall boundary condition, and the temperature
304 was set to 573 K.

306

307 2.5 Solution Methods

308

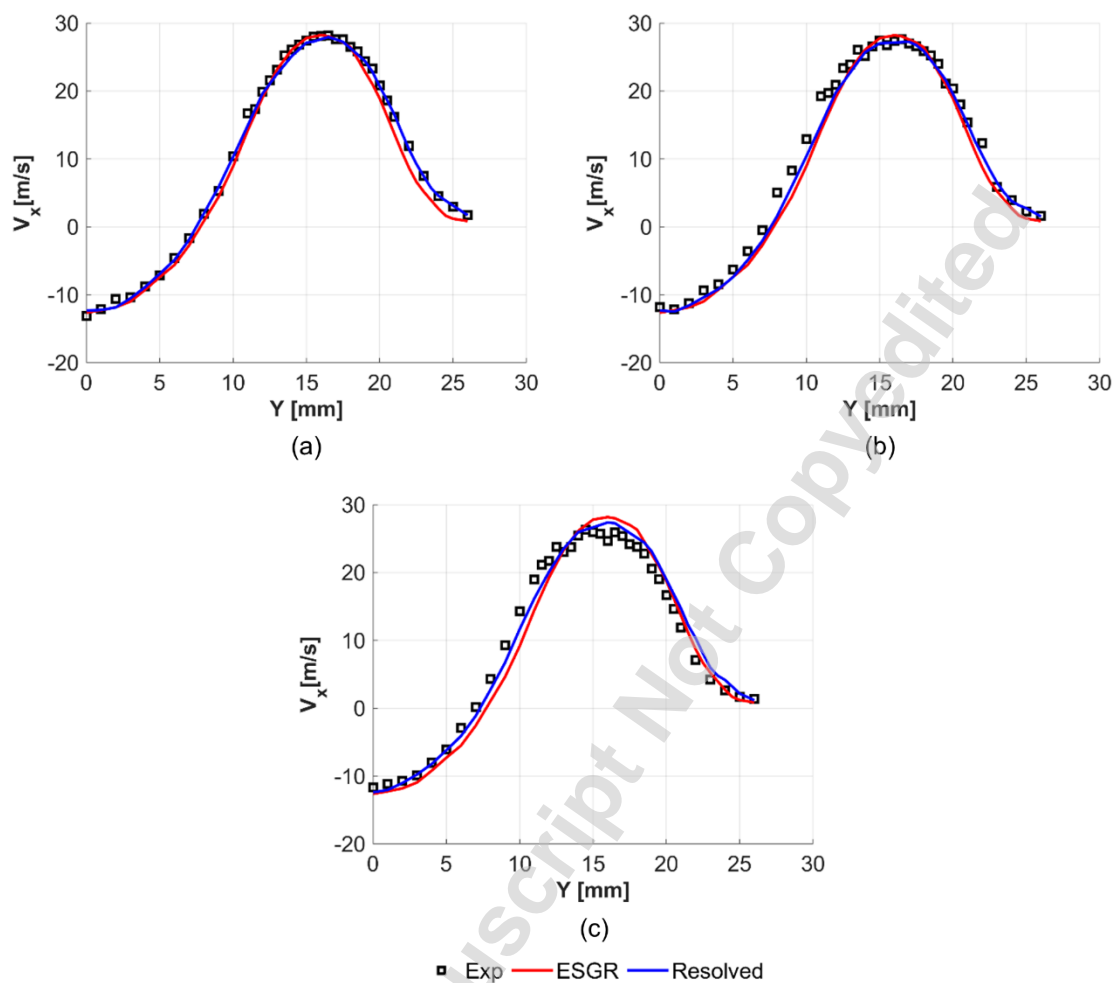
309 The solution has been calculated using the governing equations of three-
310 dimensional, incompressible flow inside the burner and Realizable k - ϵ turbulence

311 model equations were discretized over the computational cells and iteratively
312 solved by using the software. The pressure-based coupled algorithm for pressure-
313 velocity coupling, second-order upwind scheme for spatial discretization of the
314 governing equations and Green-Gauss Node for evaluation of gradients and
315 derivatives. PRESTO! interpolation scheme was applied to the model for
316 calculating pressure values at the cell faces as it performs well with high Reynolds
317 flows and high swirling flows [27, 34]. In the numerical model, the convergence
318 criteria were met by monitoring the axial flow velocity component, especially at
319 locations with significant velocity gradients. Additionally, the residuals of the
320 governing equations were required to have an absolute convergence criterion of
321 10^{-4} . For faster convergence, the global time step formulation for the pseudo time
322 method was used and the time scale factor was set initially to 10^{-4} . It was gradually
323 increased once the solution stabilised and converged smoothly.

324 3. RESULTS AND DISCUSSION

325
326 This section focuses on the results from radial locations at a fixed downstream
327 location from the nozzle exit ($X=0$, $Y=0$ and $Z=0$), as shown in Fig. 2(a).

328 Figures 5 & 6 show the predicted data for the 8M, 8G, and 8R swirl inserts. The
329 predictions are based on the modified law-of-the-wall approach using equivalent
330 sand grain roughness height (ESGR), and roughness resolving (Resolved)
331 approaches. The experimental data [8] is also included for comparison (denoted
332 as "Exp").

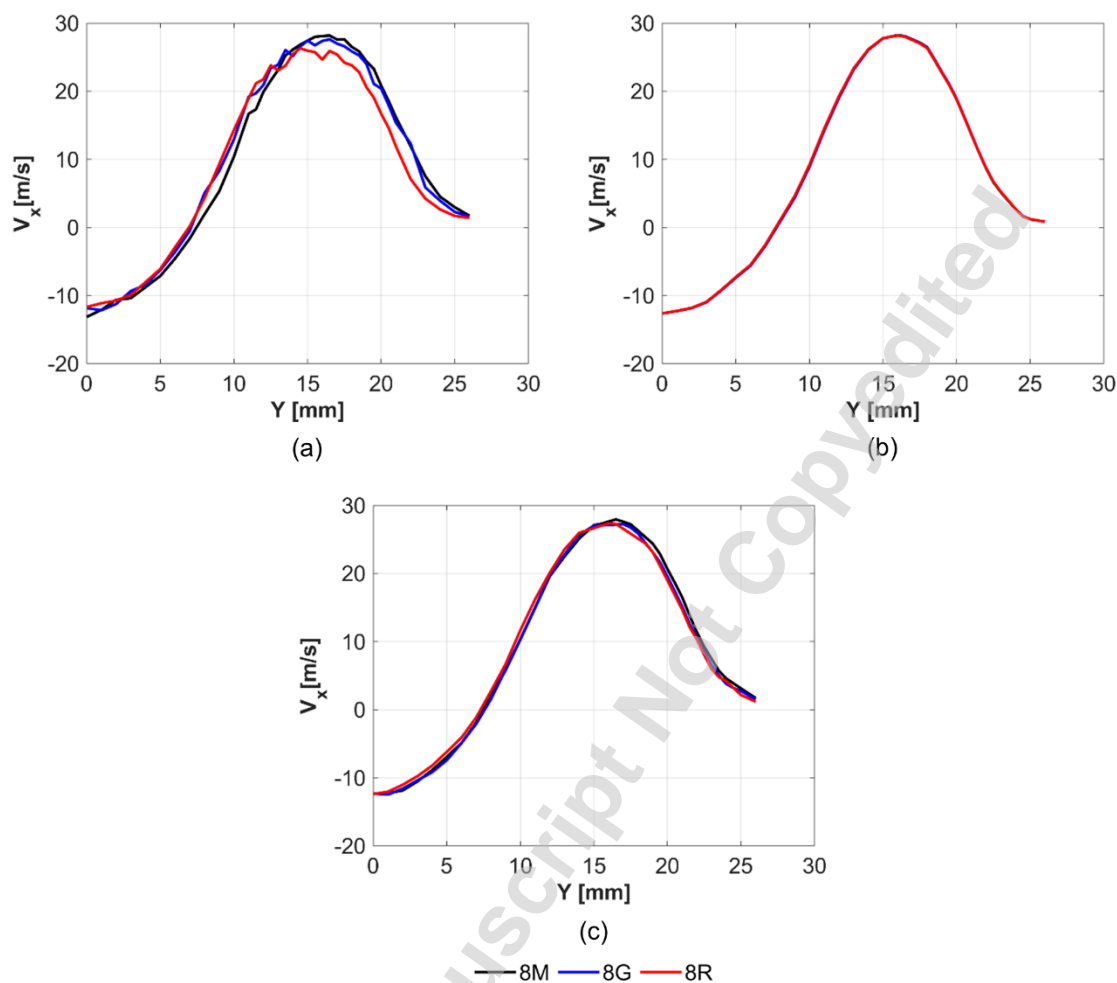


333

334 **Fig. 5** Validity of the rough modelling strategies adopted in the study at $X=5\text{mm}$ for the swirlers a)

335 8M, b) 8G, c) 8R. Experimental data are sourced from [8]. ESGR: equivalent sand-grain roughness.

336 Resolved: geometrically resolved surface roughness approach and Exp: experiment.



337

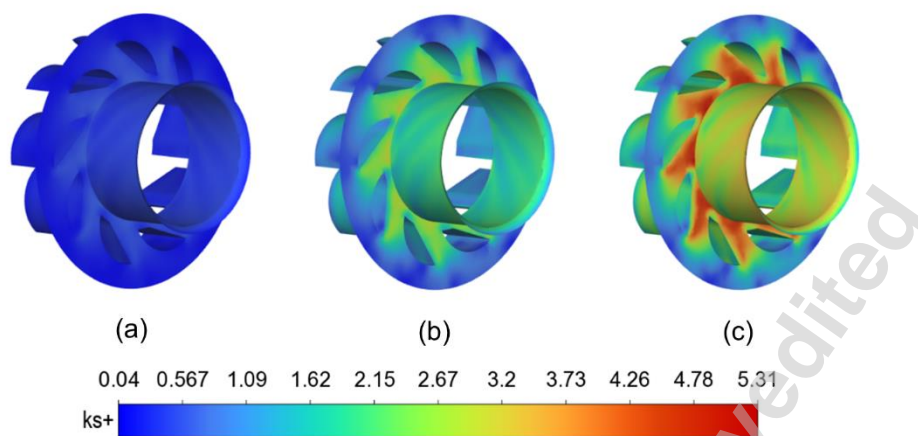
338 **Fig. 6** Validation of the wall models for the swirl inserts of “8M”, “8G” and “8R” at $X=5$ mm for (a)
 339 the experimental data, (b) the ESGR approach and (c) the geometrically resolved surface
 340 roughness approach. Experimental data are sourced from [8].

341 In the rough case (8R), both the ESGR and Resolved approaches overestimate
 342 the experimental peak velocity by 7.2% and 4.2%, respectively. The discrepancy
 343 from the experimental data becomes more noticeable in the steepest shear layers,
 344 particularly between $Y= 9$ -20 mm and $Y=20$ -24 mm. In the positive steepest shear
 345 layer ($Y=9$ -20 mm), both methods predict the velocity values, with the Resolved
 346 model exhibiting an average discrepancy of 9.2%, while the ESGR model shows

347 a larger average discrepancy of 13.8%. Conversely, in the negative steepest shear
348 layer ($Y=20-24\text{mm}$), the ESGR method outperforms the Resolved model,
349 achieving an average discrepancy of 14.5% from the experimental data. In
350 contrast, the Resolved model displays a much higher average discrepancy of
351 32.8%.

352 The results indicate that the ESGR based approach struggles to accurately predict
353 the mean velocity shift with relative roughness height in the positive shear layer.
354 This is likely to be due to the low accuracy of the correlation used to estimate the
355 equivalent sand-grain roughness height. On the other hand, the roughness
356 resolving approach predicts the velocity variation with the relative roughness
357 height reasonably well. In terms of computational expense time, both
358 methodologies have a similar average time per iteration for similar mesh size. For
359 the 8R case, the Resolved method has an averaged computational time of 34
360 seconds per iteration while the ESGR method demands 30 seconds per iteration.

361 The dimensionless roughness height, k_s^+ , was calculated for each surface
362 of the 8M, 8G and 8R swirlers based on the sand-grain roughness height. The
363 results are displayed in a contour map, given in Fig. 7.



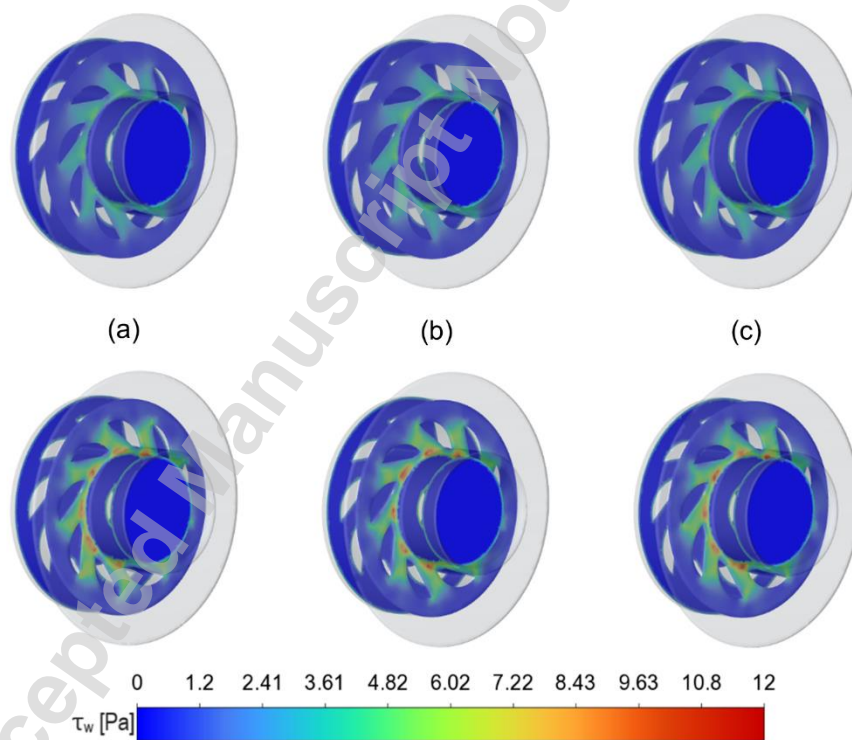
364

365 **Fig. 7** The contour of the non-dimensional roughness height, k_s^+ , calculated for (a) 8M (b) 8G and
 366 (c) 8R swirlers based on the ESGR model.

367 The values range from 0.04 to 5.31, indicating the presence of both smooth and
 368 transitional rough regimes for 8M, 8G and 8R swirlers, as defined by Cebeci and
 369 Bradshaw [31]. Note that the lower (k_s^+ smooth) and upper bands (k_s^+ rough) for
 370 the onset of transitionally rough and fully rough regimes were varied in the
 371 literature [7]. Additionally, there is no available experimental data to confirm
 372 whether the boundary layer remains in a transitionally rough regime on the wall
 373 surfaces of the swirl inserts [7]. When it comes to estimating the roughness of
 374 sand-grain surfaces, a single correlation parameter like roughness height is not
 375 enough to provide accurate results. Studies [16, 35] have shown that more
 376 complex correlations, such as those that take into account multiple roughness
 377 parameters (e.g. skewness function and effective slope), are needed to accurately
 378 estimate the roughness height for realistic surfaces. It is important to consider the
 379 3D topology of the rough surfaces in order to get a more precise estimation. The
 380 uncertainty in the correlation estimating the sand-grain roughness height could be

381 the reason why the model fails to detect the shift in velocity (Fig. 6.a) as the surface
382 height changes.

383 It has been already established [36] that the presence of surface roughness
384 above the admissible level tends to intensify the wall shear stress and the
385 thickness of the turbulent boundary layer. The extent of this impact varies with the
386 scale of the roughness [36]. Fig. 8 shows the local variation of the wall shear stress,
387 on the rough surfaces of the 8M, 8G and 8R swirlers. A comparison was made for
388 the relative roughness height and selected rough surface approaches.



389

390 **Fig. 8** Cross-sectional contour of the skin friction coefficient for the cases: (a) 8M-“ESGR”, (b) 8G-
391 “ESGR” (c) 8R- “ESGR”, (d) 8M-“Resolved,” (e) 8G-“Resolved” and (f) 8R-“Resolved”

392 Based on the contour images, the modified law-of-the wall approach doesn't
393 indicate any significant changes in τ_w concerning wall roughness height. This

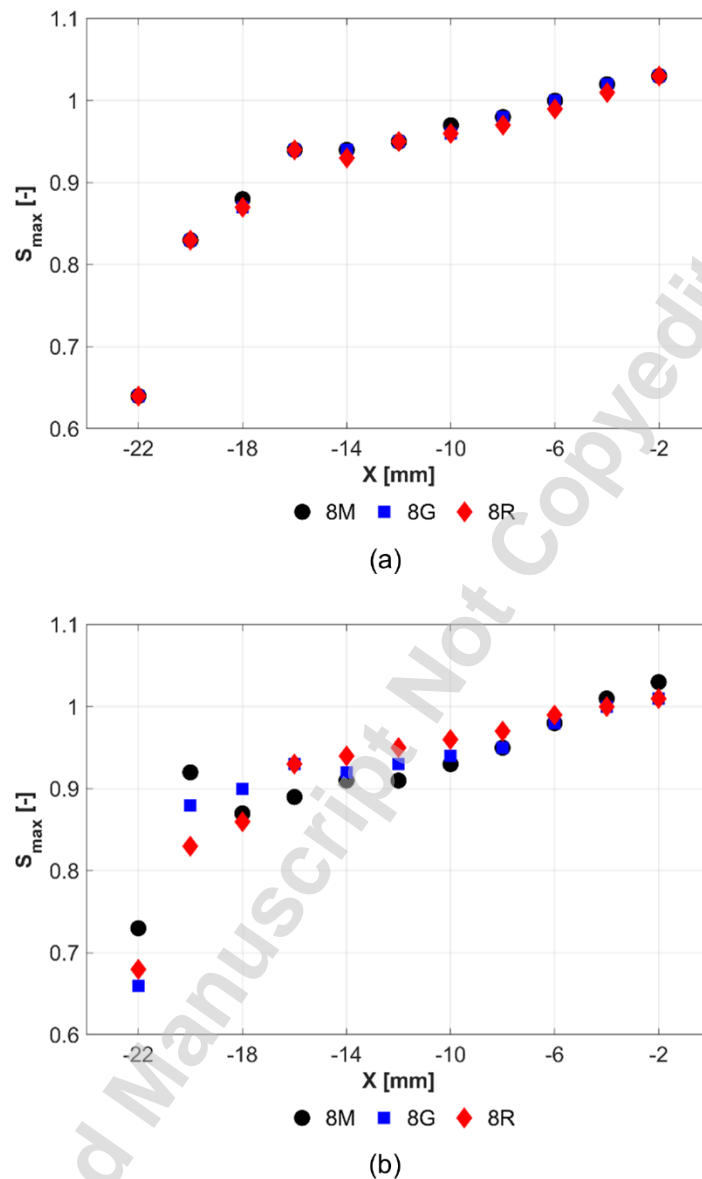
394 approach calculates the maximum values of τ_w at around 5.8 and 6.2 Pa for the
 395 8M and 8R swirlers, respectively, which differ by only 7%. However, the
 396 geometrically resolving wall roughness approach predicts that τ_w is almost twice
 397 as high for all the swirlers, with a 13% variation in the maximum values.

398 The swirling flow and thus recirculation zone inside the nozzle may be affected
 399 by the modified wall shear forces, which could explain the slight inward velocity
 400 shift with roughness height. For this reason, the swirl number, S was calculated
 401 utilising the following equation for all the CFD cases [37]:

$$402 \quad S = \frac{G_z}{R G_x} = \frac{\int_0^R \bar{V}_x \bar{V}_z r^2 dr}{R \int_0^R \bar{V}_x^2 r dr} \quad (12)$$

403 where G_z is the axial flux of swirl momentum, G_x is the axial flux of axial
 404 momentum, R is the radius, \bar{V}_x and \bar{V}_z are axial and tangential velocity component
 405 of the flow. In order to study the change in swirl number along the length of the
 406 nozzle, the maximum value of swirl number was calculated in the Y direction at
 407 every 2 mm interval in the X direction, starting from $X=-22.0$ mm and ending at $X=-$
 408 2.0 mm.

409 Fig. 9 shows the calculated maximum swirl number variation along the X
 410 direction for 8M, 8G and 8R swirl burners.



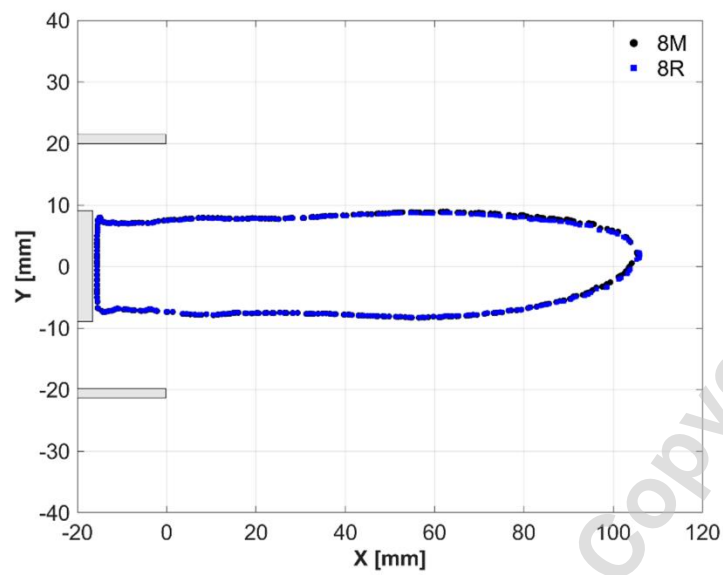
411

412 **Fig. 9** Swirl number variation in Y direction at points ranging from $X = -22$ mm to $X = -2$ mm for 8M,
 413 8G and 8R swirlers. The rectangular box bounded by a dashed line represents the bluff-body wall;
 414 a) ESGR b) Resolved.

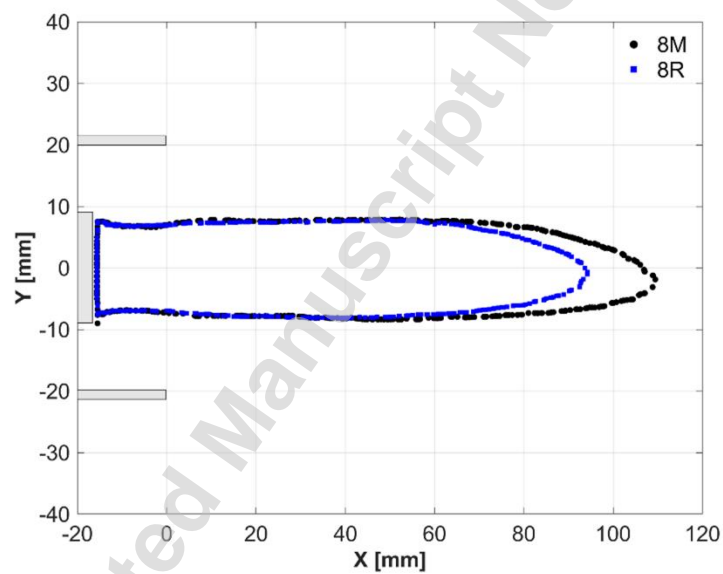
415 Within the nozzle, the swirl number deviates locally from the geometric swirl
 416 number of 0.8 for both approaches and all cases, varying along the streamwise
 417 direction. The modified law-of-the-wall approach overlaps almost entirely the swirl

418 number for all swirler inserts, indicating that surface roughness has no influence
419 on the axial and tangential velocities. On the other hand, the geometrically
420 resolved wall approach clearly predicts the local variation of the swirl number with
421 surface roughness height. At $X=-2$ mm, the 8R swirler produces lower swirling than
422 the 8M swirler, indicating a change in recirculation zone topology inside the nozzle.
423 This could well explain the inward velocity shift with surface roughness.

424 The recirculation zone topology was examined for the 8M and 8R swirlers,
425 which have significantly different maximum swirl numbers. The comparison was
426 also made for the selected approaches. The iso-profiles of the axial velocity at zero
427 were drawn to visualize the recirculation zone, as shown in Fig. 10.



(a)



(b)

428

429 **Fig. 10** Isolines of axial velocity at 0 for 8M and 8R swirlers extracted from (a) the ESGR approach
 430 and (b) the geometrically resolved wall approach.

431 As predicted, the modified law-of-the-wall approach demonstrates no
 432 variation in the central recirculation zone with the roughness height, in both the X
 433 and Y directions. On the other hand, the geometrically resolving roughness

434 approach predicts the shrinking of the recirculation zone with the surface
435 roughness height, resulting in significant shortening in the lengthwise direction.
436 The research study on high-swirl combustion [38] has uncovered a relationship
437 between NO_x emissions and the residence time within the recirculation zone. The
438 PIV results have indicated that a low-swirl injector has a weaker and smaller
439 recirculation zone, which traps a smaller recirculating mass and has a shorter
440 residence time compared to a high-swirl injector. This results in 60% less NO_x
441 produced by the low-swirl injector. The shrinking of the recirculation zone would
442 reduce the residence time and thus NO_x emissions. This has been observed in [8]
443 that an increase in surface roughness leads to a reduction in NO_x emissions, even
444 when the Adiabatic Flame Temperature and exhaust gas temperatures are similar.

445 Overall, the roughness-resolving approach has shown better performance as
446 it uses the enhanced wall treatment, addressing the near-wall zones in swirling
447 flows. This is done by smoothly blending the linear and logarithmic law-of-the-wall,
448 while also accounting for the impact of pressure gradients that are commonly
449 encountered in swirling flows. It is important to note that the predictive capability
450 of the roughness resolving method can be further improved by increasing the
451 number of roughness structures and thus the frequency of the height of roughness
452 to represent the texture of rough surfaces better [39] .

453 **4. CONCLUSIONS**

454 This study assessed the predictive capabilities of two common roughness
455 modelling strategies within the RANS approach: the Resolved and ESGR. The
456 CFD simulations were carried out for the AM generic swirl burners of different

457 surface textures and validated against published experimental data. Both
458 modelling strategies demand similar computational expense. The results
459 demonstrate that the roughness-resolving model provides better agreement with
460 the experimental data, which predicts the velocity variation with roughness height.
461 Nevertheless, both methods reveal a more noticeable discrepancy from the
462 experimental data in the steepest shear layers. The mean flow field analysis shows
463 that surface roughness shortens the recirculation zone, which can impact flame
464 stability and NO_x emissions of fuels, to be appraised in subsequent studies.

465 **ACKNOWLEDGMENT**

466 This work was supported by the UKRI Industrial Decarbonisation Research and
467 Innovation Centre (IDRIC). Rashed Al-ajmi gratefully acknowledges the receipt of
468 a scholarship from the PAAET of Kuwait during his sabbatical leave and the
469 support given by the Gas Turbine Research Center (GTRC) of Cardiff University.

470

471 **NOMENCLATURE**

472

<i>AM</i>	additive manufacturing
<i>CFD</i>	Computational Fluid Dynamics
<i>GTs</i>	Gas Turbines
<i>HPOC</i>	High Pressure Optical Combustor
<i>8G</i>	Grit blasted AM swirler
<i>8M</i>	Machined swirler
<i>8R</i>	Raw AM swirler
<i>ESGR</i>	equivalent sand grain roughness height
<i>Resolved</i>	roughness resolving
<i>Exp</i>	experimental data
A_{noz}	burner exit nozzle area (m ²)
A_{tan}	swirler tangential inlet area (m ²)
r_{noz}	burner exit nozzle radius (m)
r_{tan}	swirler effective radius of tangential inlet (m)
Q_{tan}	swirler tangential volumetric flow rate (m ³ /s)
Q_{tot}	burner exit nozzle volumetric flow rate (m ³ /s)
R_a	arithmetic average surface roughness (μm)
R_q	RMS surface roughness (μm)

R_z	ten-point mean surface roughness (μm)
S_g	geometric swirl number
K_s	equivalent sand grain roughness height (μm)
C_s	roughness constant
u_i & u_i'	mean and fluctuating velocity components
t	time
p	pressure
μ	dynamic viscosity
μ_t	turbulent viscosity
k	turbulent kinetic energy
ε	turbulent dissipation rate

473

474

REFERENCES

475

[1] ETN Global, 2020, The path towards a zero-carbon gas turbine.

476

[2] Ciani, A., Wood, J.P., Maurer, M., Bunkute, B., Pennell, D., Riazantsev, S., Früchtel, G. (2021): Center body burner for sequential combustion: Superior performance at lower emissions. In: Proceedings of the ASME Turbo Expo.

477

479

[3] Tanigawa, S., Kataoka, M., Taneike, M., Ito, R., Komaki, T., Motoyama, N., 2023, "Development of Metal AM technology for gas turbine components" Journal of the Global Power and Propulsion Society, <https://doi.org/10.33737/jgpps/163429>

480

481

482

[4] Runyon, J., Psomoglou, I., Kahraman, R., Jones, A., 2021, "Additive Manufacture and the Gas Turbine Combustor: Challenges and Opportunities to Enable Low-Carbon Fuel Flexibility", 10th International Gas Turbine Conference, Brussels, Belgium.

483

484

485

[5] Maleki, E., Bagherifard, S., Bandini, M., Guagliano, M. 2021, "Surface post-treatments for metal additive manufacturing: Progress, challenges, and opportunities",

486

- 487 Maleki, E.; Bagherifard, S.; Bandini, M.; Guagliano, M., 2020 “Surface post-treatments
488 for metal additive manufacturing: Progress, challenges, and opportunities” *Addit.*
489 *Manuf.*, 37, 101619.
- 490 [6] Bons, J.P.: A Review of Surface Roughness Effects in Gas Turbines. *J Turbomach.* 132,
491 (2010). <https://doi.org/10.1115/1.3066315>
- 492 [7] Kadivar, M., Tormey, D., & McGranaghan, G., 2021 “A review on turbulent flow over
493 rough surfaces: Fundamentals and theories” *International Journal of Thermofluids*, 10,
494 Article 100077. <https://doi.org/10.1016/j.ijft.2021.100077>
- 495 [8] Runyon, J., Giles, A., Marsh, R., Pugh, D., Goktepe, B., Bowen, P., Morris, S. 2019,
496 “Characterization of ALM Swirl Burner Surface Roughness and its Effects on Flame
497 Stability Using High-Speed Diagnostics”. *Proc. ASME Turbo. Expo.* 4A:1–13.
498 doi:10.1115/GT2019-90215.
- 499 [9] Tanneberger, T., Reichel, T.G., Krüger, O., Terhaar, S., Paschereit, C.O., 2015
500 “Numerical investigation of the flow field and mixing in a swirl stabilized burner with a
501 non-swirling axial jet” in: Volume 4B: Combustion, Fuels and Emissions, ASME,
502 Montreal, Quebec, Canada, p. V04BT04A026, <https://doi.org/10.1115/GT2015-43382>
- 503 [10] Zhu, X., Li, R., Li, D., Zhang, P., Qian, R., 2015 “Experimental study and RANS
504 calculation on velocity and temperature of a kerosene-fueled swirl laboratory
505 combustor with and without centerbody air injection” *Int J Heat Mass Transf.* 89,
506 <https://doi.org/10.1016/j.ijheatmasstransfer.2015.05.061>
- 507 [11] Mansouri, Z., Boushaki, T. 2018, “Experimental and numerical investigation of
508 turbulent isothermal and reacting flows in a non-premixed swirl burner” *Int J Heat Fluid*
509 *Flow.* 72, 200–213 (). <https://doi.org/10.1016/J.IJHEATFLUIDFLOW.2018.06.007>
- 510 [12] Chung, D., Hutchins, N., Schultz, M.P., Flack, K.A., 2021 “Predicting the Drag of
511 Rough Surfaces” *Review of Fluid Mechanics* 53 (1), 439–471
- 512 [13] Sun, W., Ma, X., Ma, S., Zhang, H., Zhang, L., Xue, H., Jia, L. 2021 “Effects of surface
513 roughness and temperature on non-equilibrium condensation and entrainment
514 performance in a desalination-oriented steam ejector” *Appl Therm Eng.* 196,
515 <https://doi.org/10.1016/j.applthermaleng.2021.117264>
- 516 [14] Orych, M., Werner, S., Larsson, L., 2022 “Roughness effect modelling for wall
517 resolved RANS – Comparison of methods for marine hydrodynamics” *Ocean*
518 *Engineering.* 266, <https://doi.org/10.1016/j.oceaneng.2022.112778>
- 519 [15] De Marchis, M., Saccone, D., Milici, B., Napoli, E. 2020, “Large Eddy Simulations of
520 Rough Turbulent Channel Flows Bounded by Irregular Roughness: Advances Toward a
521 Universal Roughness Correlation” *Flow Turbulence Combust* 105,
522 <https://doi.org/10.1007/s10494-020-00167-5>

- 523 [16] Forooghi, P., Stroh, A., Magagnato, F., Jakirlić, S., Frohnapfel, B. 2017 “Toward a
524 Universal Roughness Correlation” *Journal of Fluids Engineering, Transactions of the*
525 *ASME*. 139, <https://doi.org/10.1115/1.4037280>
- 526 [17] Coleman, H.W., Hodge, B.K., Taylor, R.P. 1984 “A re-evaluation of schlichting’s
527 surface roughness experiment” *Journal of Fluids Engineering, Transactions of the ASME*.
528 106, <https://doi.org/10.1115/1.3242406>
- 529 [18] Bons, J.P., McClain, S.T., Wang, Z.J., Chi, X., Shih, T.I. 2008 “A comparison of
530 approximate versus exact geometrical representations of roughness for CFD calculations
531 of cf and St” *Journal of Turbomachinery* 130 (2), <https://doi.org/10.1115/1.2752190>
- 532 [19] Boyle, R.J., Senyitko, R.G. 2003 “Measurements and Predictions of Surface
533 Roughness Effects on Turbine Vane Aerodynamics” In: *American Society of Mechanical*
534 *Engineers, International Gas Turbine Institute, Turbo Expo (Publication) IGTI*
- 535 [20] Taylor, J.B., Carrano, A.L., Kandlikar, S.G. 2005, “Characterization of the effect of
536 surface roughness and texture on fluid flow - Past, present, and future” In: *Proceedings*
537 *of the 3rd International Conference on Microchannels and Minichannels*.
- 538 [21] Tanneberger, T., Reichel, T.G., Krüger, O., Terhaar, S., Paschereit, C.O. 2015
539 “Numerical investigation of the flow field and mixing in a swirl stabilized burner with a
540 non-swirling axial jet” In: *Proceedings of the ASME Turbo Expo*
- 541 [22] Sawssen Chakchak A. Hidouri, A.G.M.C., Boushaki, T. 2023, “Numerical Study of
542 Turbulent Swirling Diffusion Flame Under Lean and Rich Conditions Using Turbulence
543 Realizable k-epsilon Model” *Combustion Science and Technology*. 195, 1461–1482,
544 <https://doi.org/10.1080/00102202.2023.2182196>
- 545 [23] del Olmo D’iaz, D., Hinz, D.F. 2015 “Performance of eddy-viscosity turbulence
546 models for predicting swirling pipe-flow: Simulations and laser-Doppler velocimetry”
547 arXiv: Fluid Dynamics.
- 548 [24] Mansouri, Z., Boushaki, T. 2018, “Experimental and numerical investigation of
549 turbulent isothermal and reacting flows in a non-premixed swirl burner” *Int J Heat Fluid*
550 *Flow*. 72, 200–213, <https://doi.org/10.1016/J.IJHEATFLUIDFLOW.2018.06.007>
- 551 [25] Runyon, J., Marsh, R., Bowen, P., Pugh, D., Giles, A., Morris, S. 2018 “Lean methane
552 flame stability in a premixed generic swirl burner: Isothermal flow and atmospheric
553 combustion characterization” *Exp Therm Fluid Sci*. 92,
554 <https://doi.org/10.1016/j.expthermflusci.2017.11.019>
- 555 [26] Pugh, D., Bowen, P., Valera-Medina, A., Giles, A., Runyon, J., Marsh, R. 2019,
556 “Influence of steam addition and elevated ambient conditions on NO x reduction in a
557 staged premixed swirling NH₃/H₂ flame” *Proceedings of the Combustion Institute*. 37,
558 <https://doi.org/10.1016/j.proci.2018.07.091>
- 559 [27] ANSYS Inc., 2023, *Ansys Fluent Theory Guide 23 R1*.

- 560 [28] CLAUSER, F.H. 1954 "Turbulent Boundary Layers in Adverse Pressure Gradients"
561 Journal of the Aeronautical Sciences. 21, <https://doi.org/10.2514/8.2938>
- 562 [29] Hama, F. 1954 "Boundary-layer characteristics for smooth and rough surfaces.
563 Transactions" The Society of Naval Architects and Marine Engineers, 62
- 564 [30] ANSYS Inc., 2023, FLUENT User's Guide 23 R1.
- 565 [31] Cebeci, T., Bradshaw, P., 1977, "Momentum transfer in boundary layers",
566 Hemisphere, Washington DC, 319-321.
- 567 [32] Adams, T., Grant, C., Watson, H., 2012, "A Simple Algorithm to Relate Measured
568 Surface Roughness to Equivalent Sand-grain Roughness", International Journal of
569 Mechanical Engineering and Mechatronics. <https://doi.org/10.11159/ijmem.2012.008>
- 570 [33] ANSYS FLUENT, 2009, 12.0 UDF Manual,
- 571 [34] Flack, K.A., Schultz, M.P. 2010, "Review of hydraulic roughness scales in the fully
572 rough regime", ASME. J. Fluids Eng.; 132(4): 041203. <https://doi.org/10.1115/1.4001492>
- 573 [35] Flack, K.A., Schultz, M.P., 2014 "Roughness effects on wall-bounded turbulent
574 flows". Physics of Fluids. 26, <https://doi.org/10.1063/1.4896280>
- 575 [36] Gupta, A.K., Lilley, D.G., Syred, N. 1984, "Swirl Flows" Abacus Press. Tunbridge
576 Wells, England.
- 577 [37] Johnson, M.R., Littlejohn, D., Nazeer, W.A., Smith, K.O., Cheng, R.K., 2005, "A
578 comparison of the flowfields and emissions of high-swirl injectors and low-swirl injectors
579 for lean premixed gas turbines". Proceedings of the Combustion Institute. 30 II,
580 <https://doi.org/10.1016/j.proci.2004.07.040>
- 581 [38] Tu, J., Yeoh, G.-H., Liu, C. 2018 "Chapter 7 - Practical Guidelines for CFD Simulation
582 and Analysis", In: Tu, J., Yeoh, G.-H., and Liu, C. (eds.) Computational Fluid Dynamics
583 (Third Edition). pp. 255–290. Butterworth-Heinemann
- 584 [39] Raja, J., Muralikrishnan, B., Fu, S. 2002, "Recent advances in separation of
585 roughness, waviness and form", Precis Eng. 26, [https://doi.org/10.1016/S0141-6359\(02\)00103-4](https://doi.org/10.1016/S0141-6359(02)00103-4)
- 587
- 588

589

Figure Captions List

- Fig. 1 Geometrical representation of HPOC rig without flame confinement tube
- Fig. 2 (a) Computational domain with dimensions and tagged boundaries, and
(b) Built-in tetrahedral mesh
- Fig. 3 (a) Computational domain with dimensions and tagged boundaries, and
(b) Built-in tetrahedral mesh
- Fig. 4 Grid Independency study for the modified law-of-the-wall applied to the
8M swirler
- Fig. 5 Validity of the rough modelling strategies adopted in the study at $X=5\text{mm}$
for the swirlers a) 8M, b) 8G, c) 8R. Experimental data are sourced from
[8]. ESGR: equivalent sand-grain roughness. Resolved: geometrically
resolved surface roughness approach and Exp: experiment.
- Fig. 6 Validation of the wall models for the swirl inserts of “8M”, “8G” and “8R”
at $X=5\text{mm}$ for (a) the experimental data, (b) the ESGR approach and (c) the
geometrically resolved surface roughness approach. Experimental data
are sourced from [8]
- Fig. 7 The contour of the non-dimensional roughness height, ks^+ , calculated for
(a) 8M (b) 8G and (c) 8R swirlers based on the ESGR model
- Fig. 8 Cross-sectional contour of the skin friction coefficient for the cases: (a)
8M-“ESGR”, (b) 8G-“ESGR” (c) 8R- “ESGR”, (d) 8M-“Resolved,” (e) 8G-
“Resolved” and (f) 8R-“Resolved”

Fig. 9 Swirl number variation in Y direction at points ranging from $X=-22$ mm to $X=-2$ mm for 8M, 8G and 8R swirlers. The rectangular box bounded by a dashed line represents the bluff-body wall; a) ESGR b) Resolved

Fig. 10 Isolines of axial velocity at 0 for 8M and 8R swirlers extracted from (a) the ESGR approach and (b) the geometrically resolved wall approach

590

591

Accepted Manuscript Not Copyedited

592

Table Caption List

593

Table 1 Tetrahedral mesh size used for the grid sensitivity study

Table 2 Statistics of the surface roughness based on R_z .

594

Accepted Manuscript Not Copied